Universal entrainment mechanism controls contact times with motile cells

Arnold J. T. M. Mathijssen
Department of Bioengineering, Stanford University, 443 Via Ortega, Stanford, California 94305, USA

Raphaël Jeanneret* and Marco Polin†
Physics Department, University of Warwick, Gibbet Hill Road, Coventry CV4 7AL, United Kingdom

(Received 20 July 2017; published 20 March 2018)

Contact between particles and motile cells underpins a wide variety of biological processes, from nutrient capture and ligand binding to grazing, viral infection, and cell-cell communication. The window of opportunity for these interactions depends on the basic mechanism determining contact time, which is currently unknown. By combining experiments on three different species—*Chlamydomonas reinhardtii*, *Tetraselmis subcordiforms*, and *Oxyrrhis marina*—with simulations and analytical modeling, we show that the fundamental physical process regulating proximity to a swimming microorganism is hydrodynamic particle entrainment. The resulting distribution of contact times is derived within the framework of Taylor dispersion as a competition between advection by the cell surface and microparticle diffusion, and predicts the existence of an optimal tracer size that is also observed experimentally. Spatial organization of flagella, swimming speed, and swimmer and tracer size influence entrainment features and provide tradeoffs that may be tuned to optimize the estimated probabilities for microbial interactions like predation and infection.

DOI: 10.1103/PhysRevFluids.3.033103

I. INTRODUCTION

The wide variety of microbial interactions is often deeply influenced by physics. Within biofilms, electric currents can coordinate cellular metabolic rates [1], while wrinkles draw nutrients by capillarity [2]. Microscopic flow fields [3–5] can lead to large-scale collective motion [6–9] with enhanced drug resistance [10,11], surprising rheological properties [12–14], and global features controllable by structured confinement [15–19]. When coupled with population-wide taxis, these flows result in macroscopic instabilities [20–22] which increase nutrient fluxes [23] and can provide unexpected new avenues for capture and manipulation of small objects [24].

For swimming microorganisms, many interactions hinge on close contact. These include fundamental processes like nutrient uptake [25–32]; viral and fungal infection of microorganisms of ecological and commercial importance [33–35]; eukaryotic fertilization [36]; and grazing, which happens on natural prey [31,37–39] as well as marine microplastics [40,41], and was recently discovered as a fundamental behavior in many strains of motile green algae, formerly regarded as exclusive phototrophs [35,42,43]. With the exception of complex feeding currents in ciliates like *Vorticella* [44,45] or *Paramecium* [46,47], the window of opportunity for these microbial interactions to take place will depend on a finite contact time T. For a constant success rate per unit time Ω,

*Current address: IMEDEA, University of the Balearic Islands, Carrer de Miquel Marquès, 21 07190 Esporles, Illes Balears.
†Corresponding author: M.Polin@warwick.ac.uk

the probability that the interaction is successful is given by $p(T) = 1 - e^{-\Omega T}$ [39]. Large values of $p(T)$ will be favored by long contact times, and will therefore depend on the physics that regulates proximity. Although the theoretical basis of contact times is still developing [48–50], it is reasonable to expect that a key role will be played by the properties of the near field, the region close to the cell body [31]. As already noted in this context by Purcell [51], the fluid layer close to a swimming microorganism is expected to be carried along by it. Small objects sufficiently close to a microswimmer are therefore entrained [52] and stay in close contact with it for the time required to escape the near-field region. Entrainment converts a temporal quantity, the contact time T, into a readily measurable spatial quantity, the entrainment length L. While recent studies have provided numerical support for particle entrainment by microorganisms [53–55], experimental evidence is limited to the microalga *Chlamydomonas reinhardtii* [56], and it is not clear whether or not this phenomenon is a general feature of microbial motility. At the same time, there are currently no theoretical predictions for the duration of these contact events, as a clear picture of the physics underlying entrainment is lacking [53–58].

Here we combine experimental, numerical and theoretical approaches to investigate particle entrainment by microorganisms. Experiments with the green microalgae *Chlamydomonas reinhardtii* (CR) and *Tetraselmis subcordiforms* (TS), pulled by different numbers of anterior flagella, and the dinoflagellate *Oxyrrhis marina* (OM), pushed by a posterior flagellum, demonstrate that entrainment is indeed a robust generic feature among swimming cells, whose existence is independent of the propulsion strategy. Entrainment is shown to be a direct consequence of two universal traits: advection by a no-slip cell surface, as recently suggested in [54], and particle diffusion. A first-passage Taylor-dispersion argument combines these fundamental physical ingredients, allowing for analytical estimates of the mean contact time and the full entrainment distribution, while offering an intuitive understanding of the observed existence of an optimal particle size for entrainment. We conclude by discussing potential consequences on the probability of successful interactions.

II. NEARBY-OBJECT–MICROSWIMMER INTERACTIONS ARE GOVERNED BY A UNIVERSAL ENTRAINMENT MECHANISM

When inspecting tracer dynamics at large magnification ($\times 100$) and high framerate (500 fps), very similar entrainment events are observed for all our organisms, regardless of their propulsion mechanism or generated flow. Examples of typical trajectories with particle radius $r_\mathrm{P} = 0.5\,\mu$m are shown in Movies S1–S3, for CR, TS, and OM respectively; see Supplemental Material (SM) online [59]. This mechanism is best understood from the viewpoint comoving with the swimmer. After an almost head-on collision, a bead reaches a region near the cell surface; see Fig. 1(a). It travels slowly around the body approximately following streamlines from front to back, and eventually leaves behind the organism; see Figs. 1(b) and 1(c). Since the only common physical feature of these organisms is the presence of the cell body surface, we propose that entrainment is only the consequence of the *no-slip* layer that this boundary induces. Therefore, the particle is hydrodynamically coupled to the swimmer in this layer and resides in its vicinity for an extended duration, the contact time T. In the laboratory frame, the particle is then displaced a distance L in the direction of motion. Hence, the average contact time and entrainment length are directly related via

$$\langle L \rangle \simeq v_\mathrm{S} \langle T \rangle. \tag{1}$$

To quantify our observations, we measure the distribution of L for different swimmers; see Fig. 1(e) and inset. These have all a similar shape, indicating a common underlying mechanism, with an exponential-like decay of length scale $L_\mathrm{J}^{(\mathrm{S})}$ above the length $L_\mathrm{M}^{(\mathrm{S})}$ at the peak of the distribution. Exponential fits to these curves give $L_\mathrm{J}^{(\mathrm{CR})} = 9.2 \pm 0.6\,\mu$m for CR, $L_\mathrm{J}^{(\mathrm{TS})} = 7.4 \pm 1.2\,\mu$m for TS, and $L_\mathrm{J}^{(\mathrm{OM})} = 11.7 \pm 1.4\,\mu$m for OM, while we find $L_\mathrm{M}^{(\mathrm{CR})} \approx 6.7\,\mu$m, $L_\mathrm{M}^{(\mathrm{TS})} \approx 8.6\,\mu$m, and $L_\mathrm{M}^{(\mathrm{OM})} \approx 7.5\,\mu$m.

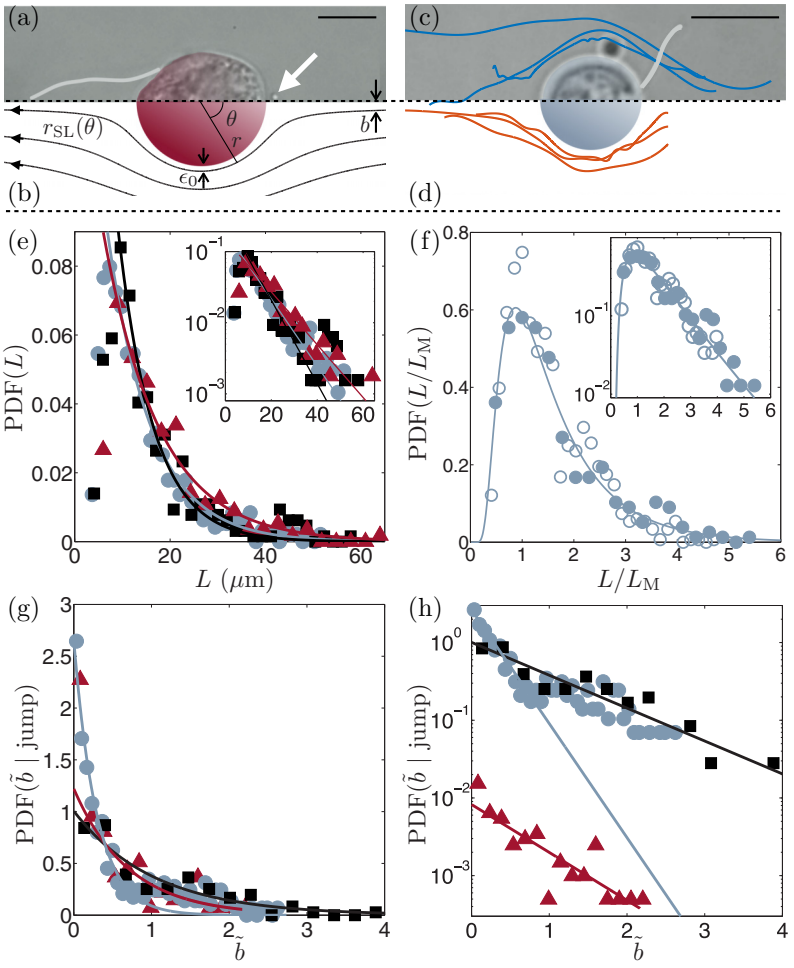

FIG. 1. (a) Snapshot of typical particle entrainment events for OM. The colloid ($r_P = 0.5\,\mu$m) is shown with a white arrow. Scale bar: $10\,\mu$m. (b) Diagram and approximated streamlines $r_{SL}(\theta) = r_S + b\sqrt{2/3}/\sin(\theta)$ of the swimmer-generated flow in its comoving frame. (c) [resp. (d)] Typical experimental [resp. numerical] tracer trajectories in the frame of CR. Scale bar: $10\,\mu$m. (e) PDF of entrainment length L obtained with tracers of radius $r_P = 0.5\,\mu$m for three different organisms: red triangles: OM; grey circles: CR; black squares: TS. Above a peak at value $L_M^{(S)}$, those are well fitted by an exponential distribution (phenomenological) with characteristic length scale $L_J^{(S)}$. Inset: semi-log plot of the same data. (f) Comparison of experimental (filled grey circles) and numerical (empty grey circles) jump length distributions using our outboard CR, for small impact parameters and normalized by L_M, the length at the maximum: $L_M^{(sim)} \approx 14.5\,\mu$m and $L_M^{(exp)} \approx 9.4\,\mu$m. The best fit using Eq. (19) (solid line) agrees well with the experimental data. Inset: semi-log plot of the same data. (g) Conditional PDF of the rescaled impact parameter $\tilde{b} = 2b/w$ given an entrainment event PDF($\tilde{b}$ | jump). Curves are fitted by exponential distributions with characteristic lengths $\tilde{b}^{(TS)} = 1.0 \pm 0.3$, $\tilde{b}^{(CR)} = 0.30 \pm 0.05$, and $\tilde{b}^{(OM)} = 0.70 \pm 0.25$. The color code is the same as in (e). (h) The same data in a semi-log plot with the curve for OM (red triangles) shifted to highlight the two regimes in the distribution for CR (grey circles).

Unexpectedly, the characteristic entrainment length $L_J^{(S)}$ is significantly smaller for TS than CR despite a slightly larger body size. As described also in SM Sec. II [59], this effect is mainly attributed to the larger number of flagella in TS, which limit the average contact time by either rapidly pushing the beads backwards during the power stroke (Movie S2) or by ejecting them out of the no-slip layer

during the recovery stroke. However, at the same time, front-mounted flagella can reach out and pull beads towards the body, widening the effective cross section for entrainment around the swimming path. This is reflected in PDF($\tilde{b}\,|\,$jump), the distribution of rescaled impact parameters, $\tilde{b} = 2b/w$, before entrainment. For both TS and OM, PDF($\tilde{b}\,|\,$jump) can be described accurately by a single exponential decay with characteristic lengths $\tilde{b}^{(\mathrm{TS})} = 1.0 \pm 0.3$ and $\tilde{b}^{(\mathrm{OM})} = 0.70 \pm 0.25$ [Figs. 1(g) and 1(h)]. However, with CR, structurally very similar to TS but with a single pair of flagella, the distribution shows two markedly distinct behaviors for impact parameters above and below the cell body radius. For $\tilde{b} > 1$, PDF($\tilde{b}\,|\,$jump) follows the curve characteristic of TS; below that threshold we observe instead an exponential decay with a significantly smaller characteristic length $\tilde{b}^{(\mathrm{CR})} = 0.30 \pm 0.05$. This is a consequence of the fact that, in CR, entrainments below $\tilde{b} \sim 1$ are by and large a consequence of "pure" collisions with the cell body, without appreciable influence from flagella. Flagella participate instead in entrainment events with relatively large impact parameters, by increasing significantly their abundance over what would otherwise be expected. In order to study the main entrainment mechanism for CR, in the following we will focus on jump events with $\tilde{b} < 0.75$ when comparing with numerical data. These include $\sim$70% of all the entrainments observed.

Inspired by previous work [31,54,60–62] we develop a self-propelled swimmer model, named the "outboard swimmer." This name implies that all propulsion forces are transmitted to the liquid from outside the cell body, as opposed to being generated at the swimmer surface. For example, the helical flagellum of a bacterium bears resemblance to an outboard motor, while CR takes after a rowing boat. To capture the near-field flows of an organism, we use a finite-sized spherical body (radius r_S) with a *no-slip* boundary condition at its surface. Propulsion is achieved by a set of regularized Stokeslets outside the body, whose flow satisfies the no-slip condition on the cell body [63]. The number, arrangement, and motion of the driving forces is species specific. Instantaneous swimming speed and rotation derive from the requirement of zero net force and torque [64]. SM Secs. III,VI [59] contain a complete presentation of the model and the resulting swimmer-generated flow fields $\boldsymbol{u}(\boldsymbol{x},t)$. This model will be used to simulate an actively beating CR, a steady OM, and a steady *E. coli* (EC) bacterium for comparison. The swimmers' size and stroke-averaged speed are $r_\mathrm{S} = 3.5, 9, 0.5\,\mu$m and $v_\mathrm{S} = 84, 100, 25\,\mu\mathrm{m.s}^{-1}$ (CR, OM, EC). Tracer particles of radius r_P are advected by the swimmer-generated velocity field according to Faxén's laws, $\boldsymbol{v} = (1 + \frac{1}{6}r_\mathrm{P}^2\nabla^2)\boldsymbol{u}$, interact with the swimmer through hard-core repulsion, and diffuse with bulk diffusivity D_0 according to the Stokes-Einstein equation.

The outboard swimmer model captures the entrainment mechanism faithfully. Figures 1(c) and 1(d) show that simulated tracer trajectories reproduce well the experimental ones. In particular, we see that in both cases the particles tend to detach close to the swimming axis despite the variation in initial impact parameter, here randomly chosen in $[0, r_\mathrm{S}]$ [see also Movies S4 and S5 for CR and OM, respectively, and Movie S6 for a comparison with a model *Escherichia coli* (EC)]. More quantitatively, the PDF of entrainment lengths from simulations agrees very well with the experimental one in Fig. 1(f), when equivalent quantities are compared (i.e., the projection of the three-dimensional jump onto the focal plane). Note that the entrainment length is globally overestimated ($L_\mathrm{M}^{(\mathrm{sim})} \approx 14.5\,\mu$m and $L_\mathrm{M}^{(\mathrm{exp})} \approx 9.4\,\mu$m), which we attribute to the approximations of this minimal model and the effect of flagella as discussed above.

III. STERIC INTERACTIONS REDUCE THE CONTACT TIME OF LARGE PARTICLES

In light of these findings about the entrainment mechanism, we will now develop a simple theory to predict contact times (see also SM Sec. VII [59]). We consider small particles that do not disturb the swimming direction significantly, which is a reasonable assumption if $r_\mathrm{P} \lesssim r_\mathrm{S}$ [55] as supported also by our experiments. A streamline along the swimmer body can be approximated as

$$r_\mathrm{SL}(\theta, b) \approx r_\mathrm{S} + b\sqrt{2/3}\big/\sin\theta, \tag{2}$$

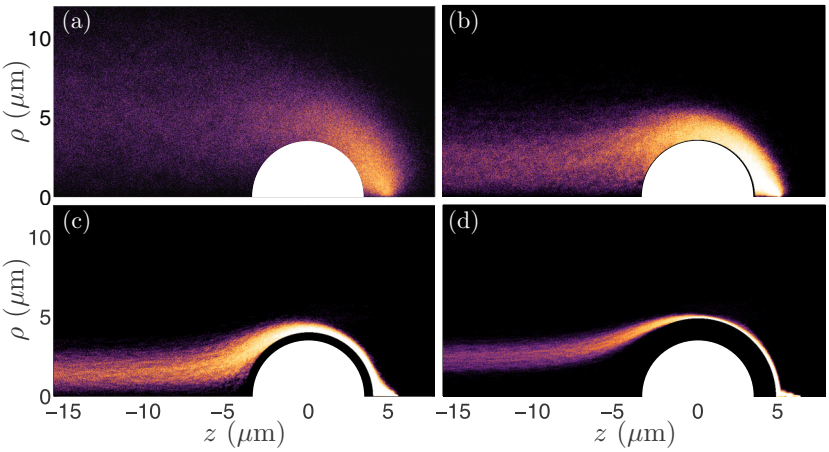

FIG. 2. Entrainment simulations by the outboard swimmer of Brownian tracer particles of various sizes. Shown are spatial PDFs of the beads, azimuthally and time averaged, as seen in the co moving frame of a CR alga, obtained by averaging over an ensemble of 10^3 particles released in front of the body at $b = 0\,\mu$m with a constant surface-to-surface distance of $1.5\,\mu$m. (a) Small tracers with $r_P = 0.01\,\mu$m diffuse away quickly and are not entrained for a long time. (b) and (c) Intermediate-sized tracers with $r_P = 0.072, 0.52\,\mu$m primarily flow along streamlines close to the swimmer body, in its no-slip layer, and are the furthest entrained. (d) Large tracers with $r_P = 1.38\,\mu$m flow along paths far from the swimmer body, and are entrained less.

written in spherical coordinates of the reference frame comoving with the swimmer; see Fig. 1(b). Close to the cell body the advection of tracers is then governed by the tangential flow, $u_\theta(r,\theta)$. Evaluating u_θ along a streamline with impact parameter b gives the velocity of a particle,

$$u_\theta[r_{SL}(b)] = \frac{3v_S\epsilon_0}{2r_S}\frac{1}{g(\lambda)} + \mathcal{O}(\epsilon_0^2), \tag{3}$$

$$g(\lambda) = \left(1 + \frac{3\lambda^3(1+\lambda)^2}{(1+2\lambda)(1+\lambda^2)^{5/2}}\right)^{-1}, \tag{4}$$

where $\epsilon_0 = r_{SL}(\pi/2) - r_S = b\sqrt{2/3}$ is the closest distance of approach [see Fig. 1(b)], and $g(\lambda) \in [0,1]$ characterises the flagellar distance from the body ($\lambda = 2,4,5$ for OM, CR and EC respectively; see SM Secs. III,V [59]). In the deterministic limit, the contact time can be calculated by integrating the inverse velocity along the particle trajectory, $T \approx \int ds/u_\theta$, where ds is the arc-length differential. Taking the streamline length as the distance that a particle must travel around the swimmer, $S = \int_{SL} ds = \pi(r_S + r_P)$ for small impact parameters, and noticing that the tangential streamline velocity Eq. (3) is constant to first order, yields the contact time in absence of fluctuations,

$$\lim_{D\to 0} T = \frac{2\pi r_S(r_S + r_P)}{3v_S\epsilon_0} g(\lambda) \tag{5}$$

$$= \frac{\sqrt{2/3}\pi r_S(r_S + r_P)}{v_S b} g(\lambda), \tag{6}$$

shown as dashed lines in Fig. 3(a) for OM, CR, and EC in the case $\epsilon_0 = r_P$. In the limit of pointlike tracer particles, $r_P \to 0$, we recover the result by Mueller and Thiffeault [54]: the entrainment length $L = v_S T = C r_S^2/b$, where the constant $C = \sqrt{2/3}\pi \sim 2.565$ for a towed no-slip sphere ($C < 2$ for typical swimmers). Interestingly, the contact time increases quadratically with the swimmer size r_S, suggesting a large difference in entrainment between bacteria and larger (eukaryotic) microorganisms, confirmed by our simulations also for finite-size particles (see Sec. IV).

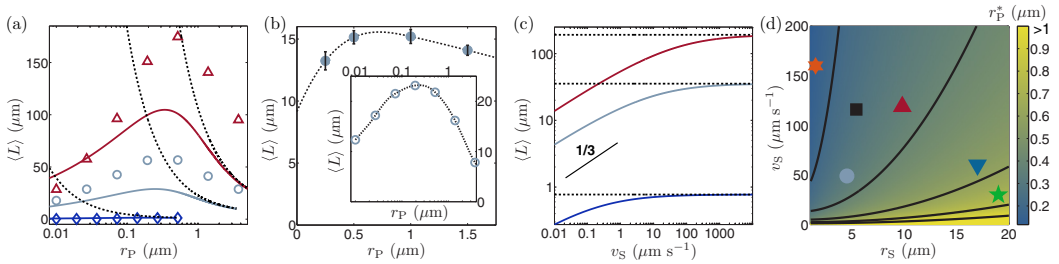

FIG. 3. Average entrainment length $\langle L \rangle$ as a function of tracer size. (a) Simulated as in Fig. 2 for OM, CR, and EC (open red triangles, grey circles, and blue diamonds respectively). The initial surface-to-surface distance is 11 μm for OM, 1.5 μm for CR, and 0.5 μm for EC. Solid lines show the corresponding analytical prediction [Eq. (15)]; dashed lines without noise [Eq. (5)]. The same data on a log-log scale are in Fig. S8(b). (b) Average entrainment length obtained experimentally with CR for different tracer sizes. The error bars represent the standard error on the mean (s.e.m.). Inset: The same data obtained in simulations with tracers initially located in front of the swimmer at impact parameters b uniformly distributed in $[0, r_S]$. Dashed lines are guides to the eye. (c) Analytical $\langle L \rangle$ as a function of swimming speed at fixed $r_P = 1$ μm. Solid lines [Eq. (15)]: OM red, CR grey, EC blue. Dashed lines [Eq. (5)]: without noise. (d) The optimal bead size r_P^* as a function of swimmer size and speed, obtained from Eq. (13) with constant value $\lambda = 4$. Markers represent a few typical model organisms—grey circle: CR; black square: TS; red pyramid: OM; blue triangle: *Euglena gracilis*; orange asterisk: *Bdellovibrio bacteriovorus*; five-pointed green star: *Peranema trichophorum*.

Overall, a small distance of approach ϵ_0 implies a slow motion around the cell body [Eq. (3)] as a consequence of the no-slip condition. As the minimum separation is dictated by the finite size of the particle, smaller tracers would naturally be expected to experience weaker tangential flows and therefore larger contact times. Yet, for any given tracer size, the estimated entrainment time [Eq. (5)] diverges with decreasing impact parameter ($\sim 1/b$) and could in principle lead to arbitrarily long entrainment events where the tracer is simply pushed like a ball on the nose of a seal, regardless of its size. This problem is solved by introducing thermal fluctuations, as we consider next.

IV. BROWNIAN NOISE LIMITS ENTRAINMENT OF SMALL PARTICLES

Together with particle advection, it is important to consider the presence of thermal noise. We first explore its effect by simulating outboard swimmers with tracers subjected to Brownian motion (Movies S4–S6 [59]). Figure 2 shows how the spatial PDF of an ensemble of tracers initially in front of the microorganism depends on tracer size. Small tracers spread far from the swimmer and do not efficiently access the no-slip layer [Fig. 2(a)]. Consequently, they are exposed to stronger tangential flows, limiting the contact time. Large tracers do not diffuse away but cannot approach the no-slip surface closely, as described previously and illustrated by the inaccessible region around the cell body [Fig. 2(d)]. Instead, we see a maximum in the contact time for beads of intermediate size, which concentrate most tightly around the moving cell [Figs. 2(b) and 2(c)]. Optimal entrainment is systematically observed in simulations of both OM and CR, with optimal tracer radii $r_P^* \sim 0.4, 0.3$ μm respectively [Fig. 3(a)]. Moreover, whereas these organisms can move particles along for $\sim$5 body lengths, entrainments by the EC model do not exceed ~ 1.2 μm for any tracer size. The superlinear growth of the average jump length on cell size (Fig. S8(c) [59] and [54]) strongly restricts particle transport for micron-size organisms, and is consistent with the lack of previous reports of strong entrainment by bacteria [65–68].

Experiments with CR for a range of different tracer sizes confirm the existence of a maximum in entrainment length [Fig. 3(b)], with diffusion-dominated tracer trajectories below and steric-interaction-limited paths above the optimal size $r_P^* \sim 0.7$ μm. These features are observed in simulations also when considering tracers that are initially located at random impact parameters b within $[0, r_S]$, rather than directly in front of the cell [Fig. 3(b) inset]. Altogether, the semiquantitative

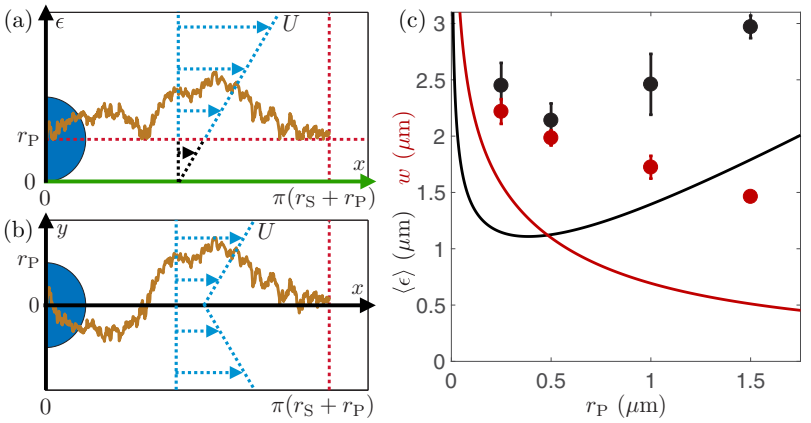

FIG. 4. Schematics of the analytical model: (a) A Brownian particle is advected over a solid surface (green axis) in a linear shear flow along the x direction characterized by a strain rate U. The tracer of radius r_P, initially located at $x = 0$ and $\epsilon = r_P$, is free to diffuse in any direction, but cannot cross the line $\epsilon = r_P$ due to steric interactions. (b) This situation is equivalent to a tracer free to diffuse through the surface $y = 0$, but with a modified flow that is nonzero at the wall and always positive. (c) Parameters $\langle\epsilon\rangle$ [black circles, Eq. (23)] and w [red circles, Eq. (26)] obtained from the fitting procedure of PDF(L), Eq. (19), for the four tracer sizes, probed with CR. The analytical estimates of these parameters (full lines) are in good semiquantitative agreement. In particular the minimum in $\langle\epsilon\rangle$ is captured at the right location.

agreement on both the location of the maximum and the values of jump lengths suggests that the outboard model captures well the essential physics behind the entrainment mechanism.

V. OPTIMAL SIZE FOR CONTACT TIME

Results from experiments and simulations can be rationalized with an approach akin to Taylor's dispersion [69,70]. Consider a Brownian particle advected in a linear shear flow over a straight solid surface that mimics the swimmer's cell wall; see Fig. 4(a). The flow velocity is $\boldsymbol{u} = \epsilon U \boldsymbol{e}_x$, where the strain rate, $U = 3v_S/(2r_S g(\lambda))$, derives from the velocity along a streamline given by Eq. (3). A particle of radius r_P is initially positioned at $(x = 0, \epsilon = r_P)$, disperses with thermal diffusivity D_0, and is advected by the flow $\boldsymbol{u}(\epsilon)$, but cannot cross the line $\epsilon = r_P$. Without loss of generality, this is mapped to an unbounded "image" system [71] where the particle is initially located at $(x = 0, y = 0)$, the modified flow is $\boldsymbol{v} = (r_P + |y|)U\boldsymbol{e}_x$, and the tracer can diffuse everywhere [Fig. 4(b)].

Our first aim is to estimate the average time $\langle T\rangle$ needed for the colloid to travel a distance $S = \pi(r_S + r_P)$ along the positive x direction, imitating a journey around the swimmer's body. The motion of the colloid is described by

$$\dot{x}(t) = (r_P + |y|)U + \xi_x(t), \quad \dot{y}(t) = \xi_y(t), \tag{7}$$

where $\boldsymbol{\xi}$ is a Gaussian white noise satisfying $\langle\xi_i\rangle = 0$ and $\langle\xi_i(t)\xi_j(t')\rangle = 2D_0\delta_{ij}\delta(t - t')$. Note that the Faxén correction for finite-sized tracer particles need not be included here, as the Laplacian acting on pure shear flows vanishes. Integrating and averaging Eq. (7) gives

$$\langle x(t)\rangle = \int_0^t dt'(r_P + \langle|y(t')|\rangle)U + \langle\xi_x(t')\rangle \tag{8}$$

$$= r_P U t + U\int_0^t dt'\left\langle\left|\int_0^{t'} dt''\xi_y(t'')\right|\right\rangle \tag{9}$$

$$= r_P U t + U\int_0^t dt'\langle|y(t')|\rangle. \tag{10}$$

Using the initial condition that particles start from $y = 0$, we can employ the canonical distribution $p(y,t) = e^{-y^2/4D_0t}/\sqrt{4\pi D_0 t}$ to give

$$\langle |y(t')| \rangle = \int_{-\infty}^{\infty} |y| p(y,t') dy = \sqrt{\frac{4D_0 t'}{\pi}}. \tag{11}$$

Inserting this expression into Eq. (10) and integrating once more then yields

$$\langle x(t) \rangle = r_P U t + \frac{4\sqrt{D_0}}{3\sqrt{\pi}} U t^{3/2}. \tag{12}$$

Requiring $\langle x(T) \rangle = S$, we find that the mean time $\langle T \rangle$ is the solution of the cubic equation

$$0 = c_0 + c_2 \langle T \rangle + c_3 \langle T \rangle^{3/2}, \tag{13}$$

$$c_0 = -\frac{2\pi r_S (r_S + r_P) g(\lambda)}{3 v_S r_P}, \quad c_2 = 1, \quad c_3 = \frac{4\sqrt{D_0}}{3 r_P \sqrt{\pi}}, \tag{14}$$

which is solved using the Cardano formula. Only one positive and real root exists for all physical situations, $c_0 < 0$ and $c_3 > 0$, which is the average contact time:

$$\langle T \rangle = \left(C_+ + C_- - \frac{c_2}{3c_3} \right)^2, \tag{15}$$

$$C_\pm = \sqrt[3]{r_C \pm \sqrt{q_C^3 + r_C^2}}, \tag{16}$$

$$q_C = -\frac{c_2^2}{9c_3^2}, \quad r_C = \frac{-27 c_0 c_3^2 - 2c_2^3}{54 c_3^3}. \tag{17}$$

The average entrainment length can then be estimated as $\langle L \rangle = v_S \langle T \rangle$, with an explicit dependence on parameters like tracer size, swimmer speed or size, temperature, and fluid viscosity. Figure 3(a) compares the results for CR, OM and EC (solid lines) when employing the same parameters used in the simulations, and shows that this simple approach recovers the correct qualitative nonmonotonic behavior of the average entrainment length, as well as the position of the entrainment maxima.

The predicted magnitude of the entrainment length deviates by a factor of ∼2 near the maxima, due mostly to an overestimate of the average tangential speed experienced by the tracer (see also Fig. S8(a) and SM Sec. VII B [59]). For either decreasing D_0 or increasing v_S, this simple estimate recovers the correct deterministic limit, in which $\langle L \rangle$ becomes independent of v_S (Fig. 3(c) dashed lines; see Eq. (5) and [54]). However, as $v_S \to 0$ thermal noise becomes important, and $\langle L \rangle \sim v_S^{1/3}$ [Fig. 3(c) solid line]: slower organisms should display shorter entrainment lengths because particles diffuse away before being displaced substantially. Altogether, these results suggest already that Brownian motion can have significant effects on the entrainment efficiency.

A simple argument can also recover the optimal tracer size r_P^* and its dependence on the swimmer's size and speed. Figure 3(d) presents a map of r_P^*, obtained by optimizing the contact time [Eq. (13)] with varying r_S and v_S but fixed $\lambda = 4$. On one hand, increasing swimmer speed v_S shifts r_P^* to lower values, because faster advection limits the importance of Brownian motion. On the other hand, increasing swimmer size r_S increases r_P^*, because the larger distance to travel around the cell enhances the relative effect of diffusion. A simple estimate for the optimal particle size is found by comparing a characteristic diffusion time $\tau_{\text{diff}} \sim r_P^2/(2D_0)$ and a characteristic advection time $\tau_{\text{adv}} \sim 2\pi r_S^2/(3 v_S r_P)$ from Eq. (3). Defining the entrainment Péclet number as $\text{Pe} = 3 v_S r_P^4/(4\pi \tilde{D}_0 r_S^2)$, where $\tilde{D}_0 = r_P D_0$, the optimal tracer size corresponds to $\text{Pe} = 1$, which yields

$$r_P^* \simeq \sqrt[4]{4\pi r_S^2 \tilde{D}_0 / 3 v_S}. \tag{18}$$

Using experimental parameter values, this expression predicts $r_P^* \sim 0.8\,\mu$m for CR, which compares well with the value $\sim 0.7\,\mu$m found experimentally, and recovers the power laws describing the dependence of r_P^* on r_S and v_S observed in numerical solutions of Eq. (13) (Fig. S9 [59]).

Notice that in many natural situations both parties can be active, and active motion of the small species could affect the duration and optimality of the contact process substantially. Considering as an example a system with a large predator and a small motile prey, the velocity v_P and reorientation timescale τ_r of the latter lead to an effective diffusion coefficients $D_{\text{active}} \sim v_P^2 \tau_r$, which can easily be $\sim$100 times larger than D_0 for typical bacteria [72,73]. The modified entrainment Péclet number can be significantly smaller than the previous one, indicating a possibly substantial decrease in contact time. Therefore, even though prey motility increases encounter rates with predators [74], it could nonetheless reduce the overall probability of being captured.

VI. THE CONTACT TIME DISTRIBUTION

The previous section provides a simple description of the average motion of a colloidal particle, based on its advection along the swimmer's body at an effective speed that depends on the particle's average distance from the swimmer. The one-dimensional (1D) parallel can in fact be pushed further to describe the whole distribution of entrainment lengths PDF(L) in Figs. 1(e) and 1(f). In the spirit of Taylor's work on diffusion within a pipe [69], the 2D motion of the entrained colloids in Fig. 4(a) and 4(b) [described by Eq. (7)] can be reduced to a 1D advection-diffusion process with an effective velocity V_{eff} and diffusivity D_{eff}.

For this system, the distribution of first arrival times T to a downstream boundary at a distance S is well known (see, e.g., [75], p. 88); and, considering the particle as a tracer being entrained by the microorganism, it can be recast as a distribution of entrainment lengths L,

$$\text{PDF}(L) = \frac{S}{\sqrt{\frac{4\pi D_{\text{eff}}}{v_S} L^3}} \exp\left(-\frac{v_S \left(S - \frac{V_{\text{eff}}}{v_S} L \right)^2}{4 D_{\text{eff}} L} \right), \tag{19}$$

where S is the length that a particle travels around the swimmer, i.e., $S = \pi(r_S + r_P)$. This functional form provides an excellent fit to *all* the experimental distributions recorded [see Fig. 1(f) and [59] Figs. S10(a) and S10(b)], confirming that the main entrainment behavior can indeed be studied within this simplified framework. The challenge is to relate the effective parameters to the experimental system. To this end, we go back to the 2D system described in Fig. 4.

A particle that starts at $(x_0 = 0, \epsilon_0 = r_P)$ will drift with an ensemble-averaged velocity V_{eff} which, after the time $\langle T \rangle$ to cross the length S [Eq. (15)], is given by

$$V_{\text{eff}}(\langle T \rangle) = \int u(\epsilon) p(\epsilon, \langle T \rangle) d\epsilon \tag{20}$$

$$= U \int \epsilon p(\epsilon, \langle T \rangle) d\epsilon \tag{21}$$

$$= U \langle \epsilon \rangle, \tag{22}$$

where $p(\epsilon, t)$ is the probability of finding the particle at a distance ϵ from the bottom wall at time t. The fitted values of V_{eff} can therefore be converted into experimental estimates for $\langle \epsilon \rangle$, and are plotted in Fig. 4(c) as black circles. Notice the minimum in the experimental values of $\langle \epsilon \rangle$, which corresponds to the optimal tracer size for entrainment. At the same time, using the canonical distribution $p(y, t)$ leads to the estimate

$$\langle \epsilon \rangle = \sqrt{\frac{4 D_0 \langle T \rangle}{\pi}} + r_P, \tag{23}$$

shown in Fig. 4(c) as a solid black line, when using the experimental CR parameters $r_S = 4.5\ \mu$m, $v_S = 49.1\ \mu\text{m.s}^{-1}$, $g(\lambda) = 0.69$ (value for the outboard CR), and $D_0 = \tilde{D}_0 / r_P$. Quantitatively, this

expression underestimates the experimental values by $\sim 1\ \mu$m, likely as a result of the approximations involved in the derivation of Eq. (23) rather than a consequence of factors like electrostatic interactions (the Debye screening length in the algal media is easily estimated to be always $\lesssim 5$ nm). Nevertheless, it recovers very well the evolution with tracer size r_P. In particular, the minima in both cases appear at the same r_P^*, and therefore Eq. (23) provides a good estimate for the optimal particle size for entrainment.

The parameter D_{eff} in Eq. (19) can be interpreted as the effective diffusivity of the particles in Fig. 4(a) along the velocity direction x. We expect this quantity to be enhanced compared to thermal diffusivity D_0 because of the background shear flow, as originally realized by Taylor for molecular diffusion within a pipe. Adapting the derivation in [76] to the case of a uniform shear flow within a thickness $l + r_P$, it is easy to show that the Brownian particles have an effective diffusivity D_{eff} along the x axis given by

$$D_{\text{eff}} = D_0\left(1 + \frac{U^2 w^4}{120 D_0^2}\right), \tag{24}$$

where $w = l - r_P$. The fitted experimental values of w are shown in Fig. 4(c) as red circles. The length scale l has been introduced in order to reduce the 2D system into an effective 1D process, and in terms of the entrainment process, it can be interpreted as the transverse length scale the beads explore before reaching the end of the body at $S = \pi(r_S + r_P)$. We therefore estimate it as the sum of the average position above the surface, plus an excess due to fluctuations given by the square root of the variance of the ϵ distribution,

$$l = \langle \epsilon \rangle + \sqrt{\langle \epsilon^2 \rangle - \langle \epsilon \rangle^2}, \tag{25}$$

evaluated at the mean contact time $\langle T \rangle$. This can be estimated analytically, and for initial condition $\epsilon_0 = r_P$ one obtains [see Eq. (11)]

$$w = \sqrt{\frac{4 D_0 \langle T \rangle}{\pi}}\left(1 + \sqrt{\frac{\pi}{2} - 1}\right). \tag{26}$$

This estimate is shown as a solid red line in Fig. 4(c): it underestimates the fitted value of w, but captures well the qualitative dependence on tracer size. The estimates in Eqs. (23) and (26) could be improved by generalizing Eq. (12) for an arbitrary initial position, and then averaging over all impact parameters, $V_{\text{eff}} = \langle V(\langle T \rangle(y_0); y_0) \rangle_{y_0}$. However, the results are not analytically tractable and therefore lose the simplicity of the minimal-model approach we focus on here, which already provides a remarkable semiquantitative description of the dynamics.

An experimentally validated model of the entrainment process allows us to rationalize experimental features of the measured distributions, and explore qualitatively their dependence on system parameters in lieu of labor-intensive experiments. On one hand, it is easy to see that the part of the distribution in Eq. (19) past the maximum can indeed be described well by a single exponential decay if the parameters provide a sufficiently large value of the effective Péclet number $\text{Pe}_{\text{eff}} = S V_{\text{eff}}/D_{\text{eff}}$. This is what we observe in Figs. 1(e) and 1(f).

VII. SUCCESS PROBABILITIES

The effective Péclet number also controls the effect of fluctuations, represented by the relative spread of the distribution of entrainment lengths, $\sqrt{\text{Var}(L)}/\langle L \rangle \sim (1/\text{Pe}_{\text{eff}})^{1/2}$. This implies that slower cells will feature a wider distribution of entrainment lengths, and therefore contact time, as the effective diffusion plays a relatively larger role than in fast-moving cells [see Fig. 5(a)]. Similarly, small tracers feature larger deviation relative to their average contact time due to the dominant effect of the effective diffusion.

In turn, these fluctuations can have some effect on the likelihood of interactions that take place during entrainment. From the contact time distribution we can analytically extract the probability of

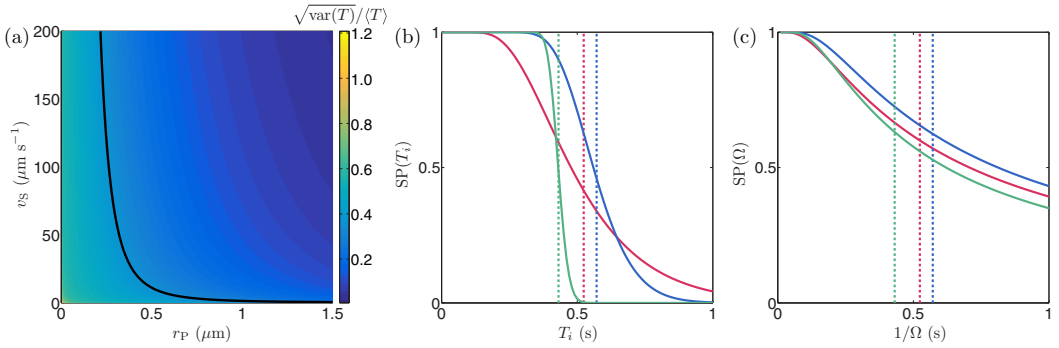

FIG. 5. Contact time fluctuations can affect the probability of a successful entrainment interaction. (a) Map of the relative width $\sqrt{\mathrm{var}(T)}/\langle T\rangle$ of the contact time distribution as a function of tracer size r_P and swimming speed v_S. Slow swimmers and small tracers show larger relative fluctuations in contact time. The solid line is the optimal tracer size for a given swimming velocity, Eq. (13). (b) and (c) Success probabilities of cell-object interactions for three different particle sizes ($r_P = 0.1\ \mu$m: pink curve; $r_P = 0.7\ \mu$m: blue curve; $r_P = 1.6\ \mu$m; green curve) in two simple cases: In (b) the interaction requires a finite time T_i to happen, and in (c) the interaction is described by a constant rate of success Ω per unit time. In the first case, fluctuations are important in setting the relative probabilities of success, while in the latter case the average contact time $\langle T\rangle$ (vertical dashed lines) mainly determines the chances of successful interaction.

success for a given cell-object interaction in two simple illustrating examples: (i) the case where the interaction requires a minimum time of contact T_i and (ii) the case of a constant success rate Ω per unit time. In the first case, the success probability (SP) is given by

$$\mathrm{SP}(T_i) = \mathrm{Prob}(T > T_i) \tag{27}$$

$$= \frac{1}{2}\left[1 + \mathrm{erf}\left(\frac{S - T_i V_{\mathrm{eff}}}{2\sqrt{D_{\mathrm{eff}} T_i}}\right) - e^{\frac{SV_{\mathrm{eff}}}{D_{\mathrm{eff}}}}\,\mathrm{erfc}\left(\frac{S + T_i V_{\mathrm{eff}}}{2\sqrt{D_{\mathrm{eff}} T_i}}\right)\right], \tag{28}$$

which is shown Fig. 5(b) for three different tracer sizes using the experimental CR parameters. For large particles the contact time does not deviate much from its average value ($\mathrm{Pe}_{\mathrm{eff}} \gg 1$), and the SP follows a switch-like dependence on the interaction time T_i (green curve), where the switching time is the average contact time $\langle T\rangle$ (dashed lines). However, as the particle size decreases below the optimal size [i.e., $r_P < r_P^*$, Eq. (18)], the fluctuations *enhance* the chance of success for slow interactions (i.e., $T_i > \langle T\rangle$), and small particles (red curve) can be more successful than those with the largest average contact time (blue curve) at slow interactions, but at the cost of reduced success for faster interactions. In the second case, the success probability is

$$\mathrm{SP}(\Omega) = \int_0^\infty (1 - e^{-\Omega T})\mathrm{PDF}(T)dT \tag{29}$$

$$= 1 - \exp\left(\frac{S\left(V_{\mathrm{eff}} - \sqrt{V_{\mathrm{eff}}^2 + 4D_{\mathrm{eff}}\Omega}\right)}{2D_{\mathrm{eff}}}\right), \tag{30}$$

shown in Fig. 5(c) for the same tracer sizes. Here we observe that fluctuations do not play a significant role. Regardless of the rate of success Ω, the chance of success will always be optimal for the tracer with the largest average contact time [Eq. (13)]. Despite their simplicity, these examples already portray the interesting role that the noisy entrainment process can play in different types of natural interactions.

VIII. CONCLUSION

Swimming microorganisms vary greatly both in body size and in the details of their propulsion, from the number and arrangement of flagella to their gaits. Yet, despite this variability, our results show that particle entrainment is a remarkably universal mechanism. Combining experiments with numerical simulations, we see that pullers and pushers entrain particles with similar efficiency. We see no evidence for either "wake bubble" effects [57], or entrainment due to a stagnation point in front of the cell [56,58]. Instead, our results suggest that entrainment is a consequence of an organism's *no-slip* surface, a characteristic shared by the three species we study here. This feature, recently suggested also in [54], is consistent with the lack of entrainment in numerical studies involving squirmers, which instead propel with a surface slip velocity [57,58]. Accordingly, we predict that ciliates like *Paramecium* and multicellular algae like *Volvox* will not substantially entrain micron-sized objects, since they swim by an effective surface slip generated by thousands of cilia and flagella. Studies of *V. carteri* swimming through a colloidal suspension support this hypothesis (see supplementary movie from [3]). Comparing different species, we also see that the flagellar arrangement has a quantitative effect on particle entrainment. Front-mounted flagella decrease the average contact time T but increase the interaction range, and are therefore likely to increase the frequency of entrainments.

The outboard model proves to be in fair qualitative and quantitative agreement with our experimental results. It provides directly comparable tracer dynamics and, crucially, it reproduces successfully the shape of the entrainment length distribution. This strongly suggests that the model captures correctly the essential physics, with further support provided by the maximum in the entrainment length over particle size observed in both experiments and simulations. These results can in fact be accurately described by a simple Taylor-dispersion theory, which provides the correct functional form for the entrainment distribution with parameters that can be estimated semiquantitatively through simple approximations. The theory, which is based exclusively on Brownian diffusion within the high-shear layer close to the swimmer's surface, provides an intuitive justification for the existence of an optimal particle size for entrainment, r_{P}^{*}, set by the balance between diffusive and advective timescales.

Size-dependent contact times might affect predation by microorganisms. Experimental studies of microbial grazing indicate that this is indeed a selective process [77]. For example, *Oxyrrhis marina* feeds on prey ranging from bacteria to cells as large as itself [37,78], but seems to have an optimal prey size [37,38,79,80], in agreement with our hydrodynamic arguments. Phagotrophic selectivity is complex, and surprisingly common even amongst microbial species historically considered exclusive autotrophs (e.g., some green microalgae [43]). It certainly depends on many factors including chemical cues and cell surface properties. However, the physics leading to the nonmonotonic size dependence of contact time is inescapable, and therefore needs to be taken into account. A nonmonotonic dependence on tracer size has also been reported for the effective diffusion of colloidal particles suspended within an *E. coli* culture [81]. These experiments, which focus on particles larger than the microorganisms, show that potentially new mechanisms could be at play in that size range.

To conclude, we have seen that particle entrainment is a generic feature of the interaction between microorganisms and small particles, and have characterized the physics behind it. A complete picture of these interactions, however, will require the integration of our results not only with those from intermediate and far-field studies [53,82], but also with a thorough characterisation of the navigational strategy of the microorganism [83]. This will enable more accurate bottom-up models of microbial grazing, which can be used to predict feeding or clearance rates by phagotrophs [31], and potential tradeoffs between feeding and swimming [26,39,84]. At the same time, prolonged contact also underpins the successful binding of viruses and other parasites to cells [33]. By showing that the contact time with motile microorganisms is limited, $\lesssim 3$ s for reasonable swimmer sizes and speeds, we suggest that motility can potentially affect infection rates [34] and thus provide a fitness advantage. This should be true in particular for ciliates, which display an effective surface slip and therefore a faster clearance of particles. Targeted experiments and modeling efforts in this area will improve our mechanistic understanding of early infection events in microorganisms.

From a microengineering perspective, our model shows that entrainment lengths become millimetric or even larger for micrometric tracers when considering swimmers or active particles with radius $r_S \gtrsim 50\,\mu$m. When combined with externally triggered reorientation events, this purely hydrodynamic phenomenon could enable cargo transport by self-propelled colloids without requiring any surface functionalization.

ACKNOWLEDGMENTS

We are grateful to Kirsty Wan and Raymond Goldstein for sharing the initial culture of TS, and to an anonymous referee for encouraging us to search for an analytic expression of the distribution of entrainment lengths. This work was supported in part by an ERC Advanced Grant (291234 MiCE) and the Human Frontier Science Program (Fellowship LT001670/2017) (A.M.), and by a Royal Society Research Grant (RG150421) (M.P.).

A.M. and R.J. contributed equally to this work and are joint lead authors. A.M., R.J., and M.P. designed the study, analyzed results, developed the theory, and wrote the manuscript; R.J. performed the experiments; A.M. developed the model and performed simulations.

APPENDIX: BRIEF DESCRIPTION OF THE EXPERIMENTAL PROCEDURES

As described in SM Sec. I, *Chlamydomonas reinhardtii* wild type strain CC125 (CR), *Tetraselmis subcordiforms* CCAP 161/1A (TS), and *Oxyrrhis marina* CCAP 1133/5 (OM) were grown respectively in tris-acetate-phosphate medium [85], seawater nutrient broth, and f/2 medium (with the alga *Nannochloropsis oculata* as food) at 21 °C under periodic fluorescent illumination (12 h/12 h). Cultures were harvested in the exponential phase ($\sim 10^6$ cells/ml for CR and TS, $\sim 10^5$ cells/ml for OM), resuspended in fresh medium, and polystyrene microparticles (Polysciences, catalog no. 19819-1) of the required radius ($r_P = 0.50 \pm 0.01\ \mu$m for TS and OM, $0.26 \pm 0.005 \leqslant r_P \leqslant 1.55 \pm 0.03\ \mu$m for CR) were added to a concentration $\lesssim 10^{-4}\%$ solids. These polystyrene particles present carboxyl groups on their surface which contribute to prevent adhesion to the microorganisms. The suspensions were then loaded into 26 μm thick (CR and TS, 29 μm thick for OM) and 5 mm wide microfluidic chambers similar to the Hele-Shaw cells used in [56]. Given the size of the organisms and the thickness of the chambers, there was enough room for the particles to travel over or beneath the swimmers around their bodies, making the entrainment mechanism fully 3D. This justifies the 3D numerical approach as the near-field flows are not expected to be influenced by the presence of confining walls. Because the colloidal suspension was very diluted and the depth of focus thick enough, we were still able to track the colloids before and after entrainment and extract accurately the entrainment lengths. We automatically extracted candidate entrainment events from long-timescale tracking of colloidal particles, followed by visual inspection to filter out spurious events. For the experiments with CR, we have extracted the following number of jump events for each particle size: 388 for $r_P = 1.5\ \mu$m, 303 for $r_P = 1\ \mu$m, 311 for $r_P = 0.5\ \mu$m, and 135 for $r_P = 0.25\ \mu$m. The three species studied have similar prolate bodies (length $l = 10.1, 13.7, 22.9\ \mu$m, width $w = 8.0, 8.4, 16.6\ \mu$m respectively for CR, TS, OM), but differ strongly in swimming mechanism. The two algal species are pulled by apical flagella, two for CR and four for TS, beating with similar waveforms but species-specific gaits: an oscillating synchronous breaststroke for CR [86] and a smooth transverse gallop for TS [87]. Both are, on average, puller-type microswimmers [4,88,89]. The dinoflagellate OM possesses two flagella at the back of its body: a short lateral one used to turn and to aid in feeding [90] and a longer one pushing the cell forward. It is therefore a pusher-type microorganism [90]. The three organisms swim with characteristic velocities $v_S = 49, 116, 119\ \mu\mathrm{m\,s^{-1}}$ (CR, TS, OM).

[1] A. Prindle, J. Liu, M. Asally, S. Ly, J. Garcia-Ojalvo, and G. M. Süel, Ion channels enable electrical communication in bacterial communities, Nature (London) **527**, 59 (2015).

[2] J. N. Wilking, V. Zaburdaev, M. De Volder, R. Losick, M. P. Brenner, and D. A. Weitz, Liquid transport facilitated by channels in Bacillus subtilis biofilms, Proc. Natl. Acad. Sci. U. S. A. **110**, 848 (2013).
[3] K. Drescher, R. E. Goldstein, N. Michel, M. Polin, and I. Tuval, Direct Measurement of the Flow Field Around Swimming Microorganisms, Phys. Rev. Lett. **105**, 168101 (2010).
[4] J. S. Guasto, K. A. Johnson, and J. P. Gollub, Oscillatory Flows Induced by Microorganisms Swimming in Two Dimensions, Phys. Rev. Lett. **105**, 168102 (2010).
[5] K. Drescher, J. Dunkel, L. H. Cisneros, S. Ganguly, and R. E. Goldstein, Fluid dynamics and noise in bacterial cell-cell and cell-surface scattering, Proc. Natl. Acad. Sci. U. S. A. **108**, 10940 (2011).
[6] H. P. Zhang, A. Be'er, E.-L. Florin, and H. L. Swinney, Collective motion and density fluctuations in bacterial colonies, Proc. Natl. Acad. Sci. U. S. A. **107**, 13626 (2010).
[7] L. H. Cisneros, R. Cortez, C. Dombrowski, R. E. Goldstein, and J. O. Kessler, Fluid dynamics of self-propelled microorganisms, from individuals to concentrated populations, Exp. Fluids **43**, 737 (2010).
[8] A. Sokolov and I. S. Aranson, Physical Properties of Collective Motion in Suspensions of Bacteria, Phys. Rev. Lett. **109**, 248109 (2012).
[9] D. Krishnamurthy and G. Subramanian, Collective motion in a suspension of micro-swimmers that run-and-tumble and rotary diffuse, J. Fluid Mech. **781**, 422 (2015).
[10] S. Lai, J. Tremblay, and E. Déziel, Swarming motility: A multicellular behavior conferring antimicrobial resistance, Environ. Microbiol. **11**, 126 (2009).
[11] M. T. Butler, Q. Wang, and R. M. Harshey, Cell density and mobility protect swarming bacteria against antibiotics, Proc. Natl. Acad. Sci. U. S. A. **107**, 3776 (2010).
[12] A. Sokolov and I. S. Aranson, Reduction of Viscosity in Suspension of Swimming Bacteria, Phys. Rev. Lett. **103**, 148101 (2009).
[13] S. Rafaï, L. Jibuti, and P. Peyla, Effective Viscosity of Microswimmer Suspensions, Phys. Rev. Lett. **104**, 098102 (2010).
[14] H. M. López, J. Gachelin, C. Douarche, H. Auradou, and E. Clément, Turning Bacteria Suspensions into Superfluids, Phys. Rev. Lett. **115**, 028301 (2015).
[15] H. Wioland, F. G. Woodhouse, J. Dunkel, J. O. Kessler, and R. E. Goldstein, Confinement Stabilizes a Bacterial Suspension into a Spiral Vortex, Phys. Rev. Lett. **110**, 268102 (2013).
[16] A. J. T. M. Mathijssen, A. Doostmohammadi, J. M. Yeomans, and T. N. Shendruk, Hotspots of boundary accumulation: dynamics and statistics of micro-swimmers in flowing films, J. R. Soc. Interface **13**, 20150936 (2016).
[17] M. Ravnik and J. M. Yeomans, Confined Active Nematic Flow in Cylindrical Capillaries, Phys. Rev. Lett. **110**, 026001 (2013).
[18] E. Lushi, H. Wioland, and R. E. Goldstein, Fluid flows created by swimming bacteria drive self-organization in confined suspensions, Proc. Natl. Acad. Sci. U. S. A. **111**, 9733 (2014).
[19] A. J. T. M. Mathijssen, A. Doostmohammadi, J. M. Yeomans, and T. N. Shendruk, Hydrodynamics of microswimmers in films, J. Fluid Mech. **806**, 35 (2015).
[20] J. R. Platt, "Bioconvection patterns" in cultures of free-swimming organisms, Science **133**, 1766 (1961).
[21] M. S. Plesset and H. Winet, Bioconvection patterns in swimming microorganism cultures as an example of Rayleigh-Taylor instability, Nature (London) **248**, 441 (1974).
[22] T. J. Pedley, N. A. Hill, and J. O. Kessler, The growth of bioconvection patterns in a uniform suspension of gyrotactic micro-organisms, J. Fluid Mech. **195**, 223 (1988).
[23] I. Tuval, L. Cisneros, C. Dombrowski, C. W. Wolgemuth, J. O. Kessler, and R. E. Goldstein, Bacterial swimming and oxygen transport near contact lines, Proc. Natl. Acad. Sci. U. S. A. **102**, 2277 (2005).
[24] J. Dervaux, M. Capellazzi Resta, and P. Brunet, Light-controlled flows in active fluids, Nat. Phys. **13**, 306 (2016).
[25] V. Magar, T. Goto, and T. J. Pedley, Nutrient uptake by a self-propelled steady squirmer, Q. J. Mech. Appl. Math. **56**, 65 (2003).
[26] S. Michelin and E. Lauga, Optimal feeding is optimal swimming for all Péclet numbers, Phys. Fluids **23**, 101901 (2011).
[27] D. Tam and A. E. Hosoi, Optimal feeding and swimming gaits of biflagellated organisms, Proc. Natl. Acad. Sci. U. S. A. **108**, 1001 (2011).

[28] A. Doostmohammadi, R. Stocker, and A.M. Ardekani, Low-Reynolds-number swimming at pycnoclines, Proc. Natl. Acad. Sci. U. S. A. **109**, 3856 (2012).
[29] R. A. Lambert, F. Picano, W.-P. Breugem, and L. Brandt, Active suspensions in thin films: Nutrient uptake and swimmer motion, J. Fluid Mech. **733**, 528 (2013).
[30] T. Ishikawa, S. Kajiki, Y. Imai, and T. Omori, Nutrient uptake in a suspension of squirmers, J. Fluid Mech. **789**, 481 (2016).
[31] J. Dölger, L. Tor Nielsen, T. Kiørboe, and A. Andersen, Swimming and feeding of mixotrophic biflagellates, Sci. Rep. **7**, 39892 (2017).
[32] M. B. Short, C. A. Solari, S. Ganguly, T. R. Powers, J. O. Kessler, and R. E. Goldstein, Flows driven by flagella of multicellular organisms enhance long-range molecular transport, Proc. Natl. Acad. Sci. U. S. A. **103**, 8315 (2006).
[33] G. Seisenberger, M. U. Ried, T. Endress, H. Büning, M. Hallek, and C. Bräuchle, Real-time single-molecule imaging of the infection pathway of an adeno-associated virus, Science **294**, 1929 (2001).
[34] T. B. Taylor and A. Buckling, Bacterial motility confers fitness advantage in the presence of phages, J. Evol. Biol. **26**, 2154 (2013).
[35] L. T. Carney and T. W. Lane, Parasites in algae mass culture, Front. Microbiol. **5**, 278 (2014).
[36] J. A. Riffell and R. K. Zimmer, Sex and flow: The consequences of fluid shear for sperm–egg interactions, J. Exp. Biol. **210**, 3644 (2007).
[37] E. C. Roberts, E. C. Wootton, K. Davidson, H. J. Jeong, C. D. Lowe, and D. J. S. Montagnes, Feeding in the dinoflagellate *Oxyrrhis marina*: Linking behavior with mechanisms, J. Plankt. Res. **33**, 603 (2010).
[38] K. Davidson, F. Sayegh, and D. J. S. Montagnes, *Oxyrrhis marina*-based models as a tool to interpret protozoan population dynamics, J. Plankt. Res. **33**, 651 (2011).
[39] W. Gilpin, V. N. Prakash, and M. Prakash, Vortex arrays and ciliary tangles underlie the feeding-swimming trade-off in starfish larvae, Nat. Phys. **13**, 380 (2017).
[40] M. Cole, P. Lindeque, E. Fileman, C. Halsband, R. Goodhead, J. Moger, and T. S. Galloway, Microplastic ingestion by zooplankton, Environ. Sci. Technol. **47**, 6646 (2013).
[41] S. L. Wright, R. C. Thompson, and T. S. Galloway, The physical impacts of microplastics on marine organisms: A review, Environ. Pollution **178**, 483 (2013).
[42] S. Maruyama and E. Kim, A modern descendant of early green algal phagotrophs, Curr. Biol. **23**, 1081 (2013).
[43] M.-A. Selosse, M. Charpin, and F. Not, Mixotrophy everywhere on land and in water: The grand écart hypothesis, Ecol. Lett. **20**, 246 (2017).
[44] R. E. Pepper, M. Roper, S. Ryu, P. Matsudaira, and H. A. Stone, Nearby boundaries create eddies near microscopic filter feeders, J. R. Soc. Interface **7**, 851 (2010).
[45] R. E. Pepper, M. Roper, S. Ryu, N. Matsumoto, M. Nagai, and H. A. Stone, A new angle on microscopic suspension feeders near boundaries, Biophys. J. **105**, 1796 (2013).
[46] I. Jung, T. R. Powers, and J. M. Valles, Evidence for two extremes of ciliary motor response in a Single swimming microorganism, Biophys. J. **106**, 106 (2014).
[47] P. Zhang, S. Jana, M. Giarra, P. P. Vlachos, and S. Jung, Paramecia swimming in viscous flow, Eur. Phys. J.-Spec. Top. **224**, 3199 (2015).
[48] M. Bally, A. Gunnarsson, L. Svensson, G. Larson, V. P. Zhdanov, and F. Höök, Interaction of Single Viruslike Particles with Vesicles Containing Glycosphingolipids, Phys. Rev. Lett. **107**, 188103 (2011).
[49] A. Banerjee, A. Berezhkovskii, and R. Nossal, Kinetics of cellular uptake of viruses and nanoparticles via clathrin-mediated endocytosis, Phys. Biol. **13**, 016005 (2016).
[50] H. Xu and D. E. Shaw, A simple model of multivalent adhesion and its application to influenza infection, Biophys. J. **110**, 218 (2016).
[51] E. M. Purcell, Life at low Reynolds number, Am. J. Phys **45**, 3 (1977).
[52] C. Darwin, Note on hydrodynamics, Math. Proc. Camb. Philos. Soc. **49**, 342 (1953).
[53] D. O. Pushkin, H. Shum, and J. M. Yeomans, Fluid transport by individual microswimmers, J. Fluid Mech. **726**, 5 (2013).
[54] P. Mueller and J.-L. Thiffeault, Fluid transport and mixing by an unsteady microswimmer, Phys. Rev. Fluids **2**, 013103 (2017).

[55] H. Shum and J. M. Yeomans, Entrainment and scattering in microswimmer-colloid interactions, Phys. Rev. Fluids **2**, 113101 (2017).
[56] R. Jeanneret, D. O. Pushkin, V. Kantsler, and M. Polin, Entrainment dominates the interaction of microalgae with micron-sized objects, Nat. Commun. **7**, 12518 (2016).
[57] Z. Lin, J.-L. Thiffeault, and S. Childress, Stirring by squirmers, J. Fluid Mech. **669**, 167 (2011).
[58] J.-L. Thiffeault, Distribution of particle displacements due to swimming microorganisms, Phys. Rev. E **92**, 023023 (2015).
[59] See Supplemental Material at http://link.aps.org/supplemental/10.1103/PhysRevFluids.3.033103 for further details on experimental methods; simulations of CR, EC, and OM within the outboard model; and size-dependent entrainment.
[60] R. R. Bennett and R. Golestanian, Emergent Run-and-Tumble Behavior in a Simple Model of *Chlamydomonas* with Intrinsic Noise, Phys. Rev. Lett. **110**, 148102 (2013).
[61] B. M. Friedrich and F. Jülicher, Flagellar Synchronization Independent of Hydrodynamic Interactions, Phys. Rev. Lett. **109**, 138102 (2012).
[62] D. R. Brumley, K. Y. Wan, M. Polin, and R. E. Goldstein, Flagellar synchronization through direct hydrodynamic interactions, eLife **3**, e02750 (2014).
[63] S. E. Spagnolie, G. R. Moreno-Flores, D. Bartolo, and E. Lauga, Geometric capture and escape of a microswimmer colliding with an obstacle, Soft Matter **11**, 3396 (2015).
[64] S. Kim and S. J. Karilla, *Microhydrodynamics* (Dover, New York, 1991).
[65] X.-L. Wu and A. Libchaber, Particle Diffusion in a Quasi-Two-Dimensional Bacterial Bath, Phys. Rev. Lett. **84**, 3017 (2000).
[66] T. Ishikawa, J. T. Locsei, and T. J. Pedley, Fluid particle diffusion in a semidilute suspension of model micro-organisms, Phys. Rev. E **82**, 021408 (2010).
[67] T. V. Kasyap, D. L. Koch, and M. Wu, Hydrodynamic tracer diffusion in suspensions of swimming bacteria, Phys. Fluids **26**, 081901 (2014).
[68] A. Jepson, V. A. Martinez, J. Schwarz-Linek, A. Morozov, and W. C. K. Poon, Enhanced diffusion of nonswimmers in a three-dimensional bath of motile bacteria, Phys. Rev. E **88**, 041002(R) (2013).
[69] G. Taylor, Dispersion of soluble matter in solvent flowing slowly through a tube, Proc. R. Soc. Lond. A **219**, 186 (1953).
[70] H. A. Stone, A. D. Stroock, and A. Ajdari, Engineering flows in small devices: Microfluidics toward a lab-on-a-chip, Annu. Rev. Fluid Mech. **36**, 381 (2004).
[71] N. G. Van Kampen, *Stochastic Processes in Physics and Chemistry* (Elsevier, Amsterdam, 1983).
[72] H. C. Berg, *Random Walks in Biology* (Princeton University Press, Princeton, 1993).
[73] J. Saragosti, P. Silberzan, and A. Buguin, Modeling *E. coli* tumbles by rotational diffusion: Implications for chemotaxis, PlOS One **7**, e35412 (2012).
[74] R. Almeda, H. van Someren Gréve, and T. Kiørboe, Behavior is a major determinant of predation risk in zooplankton, Ecosphere **8**, e01668 (2016).
[75] S. Redner, *A Guide to First-Passage Time Processes* (Cambridge University Press, Cambridge, 2001).
[76] S. C. James and C. V. Chrysikopoulos, Effective velocity and effective dispersion coefficient for finite-sized particles flowing in a uniform fracture, J. Colloid Interface Sci. **263**, 288 (2003).
[77] D. J. S. Montagnes, A. B. Barbosa, J. Boenigk, K. Davidson, K. Jürgens, M. Macek, J. D. Parry, E. C. Roberts, and K. Šimek, Selective feeding behaviour of key free-living protists: Avenues for continued study, Aquat. Microb. Ecol. **53**, 83 (2008).
[78] K. J. Flynn, K. Davidson, and A. Cunningham, Prey selection and rejection by a microflagellate; implications for the study and operation of microbial food webs, J. Exp. Marine Biol. Ecol. **196**, 357 (1996).
[79] P. J. Hansen, Prey size selection, feeding rates and growth dynamics of heterotrophic dinoflagellates with special emphasis on Gyrodinium spirale, Marine Biol. **114**, 327 (1992).
[80] F. C. Hansen, H. J. Witte, and J. Passarge, Grazing in the heterotrophic dinoflagellate *Oxyrrhis marina*: Size selectivity and preference for calcified *Emiliania huxleyi* cells, Aquat. Microb. Ecol. **10**, 307 (1996).
[81] A. E. Patteson, A. Gopinath, P. K. Purohit, and P. E. Arratia, Particle diffusion in active fluids is non-monotonic in size, Soft Matter **12**, 2365 (2016).

[82] A. J. T. M. Mathijssen, D. O. Pushkin, and J. M. Yeomans, Tracer trajectories and displacement due to a micro-swimmer near a surface, J. Fluid Mech. **773**, 498 (2015).
[83] V. Méndez, D. Campos, and F. Bartumeus, *Stochastic Foundations in Movement Ecology: Anomalous Diffusion, Front Propagation and Random Searches*, Springer Series in Synergetics (Springer, Berlin, 2013).
[84] R. R. Strathmann and D. Grünbaum, Good eaters, poor swimmers: Compromises in larval form, Integr. Compar. Biol. **46**, 312 (2006).
[85] J. D. Rochaix, S. Mayfield, M. Goldschmidt-Clermont, and J. Erickson, Molecular biology of chlamydomonas, in *Plant Molecular Biology: A Practical Approach* (IRL, Oxford, 1988), pp. 253–275.
[86] M. Polin, I. Tuval, K. Drescher, J. P. Gollub, and R. E. Goldstein, Chlamydomonas swims with two "gears" in a eukaryotic version of run-and-tumble locomotion, Science **325**, 487 (2009).
[87] K. Y. Wan and R. E. Goldstein, Coordinated beating of algal flagella is mediated by basal coupling, Proc. Natl. Acad. Sci. U. S. A. **113**, E2784 (2016).
[88] E. Lauga and T. R. Powers, The hydrodynamics of swimming microorganisms, Rep. Prog. Phys. **72**, 096601 (2009).
[89] G. S. Klindt and B. M. Friedrich, Flagellar swimmers oscillate between pusher- and puller-type swimming, Phys. Rev. E **92**, 063019 (2015).
[90] T. Kiørboe, H. Jiang, R. J. Goncalves, L. T. Nielsen, and N. Wadhwa, Flow disturbances generated by feeding and swimming zooplankton, Proc. Natl. Acad. Sci. U. S. A. **111**, 11738 (2014).